*applied sciences*

MDPI

*Article*

# Accuracy Assessment of Mesh Types in Tectonic Modeling to Reveal Seismic Potential Using the Finite Element Method: A Case Study at the Main Marmara Fault

**Mustafa Fahri Karabulut [1,*] and Vahap Engin Gülal [2]**

[1] Department of Geomatics Engineering, Yıldız Technical University, 34220 Istanbul, Turkey
[2] Department of Computer Engineering, Atlas University, 34403 Istanbul, Turkey; engin.gulal@atlas.edu.tr
* Correspondence: mfahri@yildiz.edu.tr

**Abstract:** Earthquakes occur as a result of ruptures on faults along plate boundaries. It is possible to reveal the approximate location and magnitude of the earthquake rupture, but this requires that the seismic cycle and kinematics of the study area are well known. Different measurement methods and modeling techniques are used to determine fault kinematics. Near-surface annual slip can be determined using various methods, such as the Global Navigation Satellite System (GNSS), Interferometric Synthetic Aperture Radar (InSAR), or geological studies. As a result of modeling using these methods, the slip amounts of the fault at any depth can be revealed. Interseismic modeling with the 3D Finite Element Model (FEM) is one of them. Considering the studies conducted in the literature, the effects of the discrete method of fault kinematics in the modeling performed with FEM have not been revealed. In order to fill this gap, 3D FEM modeling has been performed using velocity data from GNSS stations located around the Main Marmara Fault. The accuracy of the models made using different mesh types in ANSYS (Analysis System) software has been examined. The fault slip deficit values of the faults of the models with the lowest and highest Root Mean Square Error (RMSE) values have been compared. Possible earthquake magnitudes have been obtained after calculating the total slip deficit through taking into account the seismic gap. The moment magnitude of possible rupture difference has been revealed to be between 0.01 and 0.014 through using the lowest RMSE and the highest RMSE model.

**Keywords:** finite element method; mesh type; GNSS; modeling; seismic potential



**Citation:** Karabulut, M.F.; Gülal, V.E. Accuracy Assessment of Mesh Types in Tectonic Modeling to Reveal Seismic Potential Using the Finite Element Method: A Case Study at the Main Marmara Fault. *Appl. Sci.* **2023**, *13*, 13297. https://doi.org/10.3390/app132413297

Academic Editor: Kang Su Kim

Received: 14 November 2023
Revised: 8 December 2023
Accepted: 13 December 2023
Published: 16 December 2023



## 1. Introduction

Numerous earthquakes of varying magnitudes occur around the world along faults formed as a result of the movement of tectonic plates [1]. One of these regions is the Anatolian plate, which interacts with the African, Arabian, and Eurasian plates (Figure 1) [2,3]. There are many fault lines on this plate that have the potential to generate earthquakes. The most important of these are the North Anatolian Fault and East Anatolian Fault [2,4]. Many earthquakes of magnitude seven or greater have occurred on them [5–7].

Determining the annual slip of plate motion is of great importance in revealing the seismic potential. The amount of annual slip can be determined through the Global Navigation Satellite System (GNSS) with an accuracy of a millimeter or less [7–12]. Accordingly, the Anatolian Plate is moving westward at a rate of about 25 mm per year. Moment magnitude ($M_w$) $\geq$ 7 earthquakes have been recorded along the North Anatolian Fault during the instrumental period.

When we examine these earthquakes and their dates, there is a chain of earthquakes moving from east to west (Figure 2) [6,13,14]. The last of this series were the Düzce and Gölcük earthquakes in 1999. Therefore, studies have shown that the next earthquake will occur within the Main Marmara Fault (MMF), which is the main branch of the North Anatolian Fault in the Marmara Region [12,15–19].

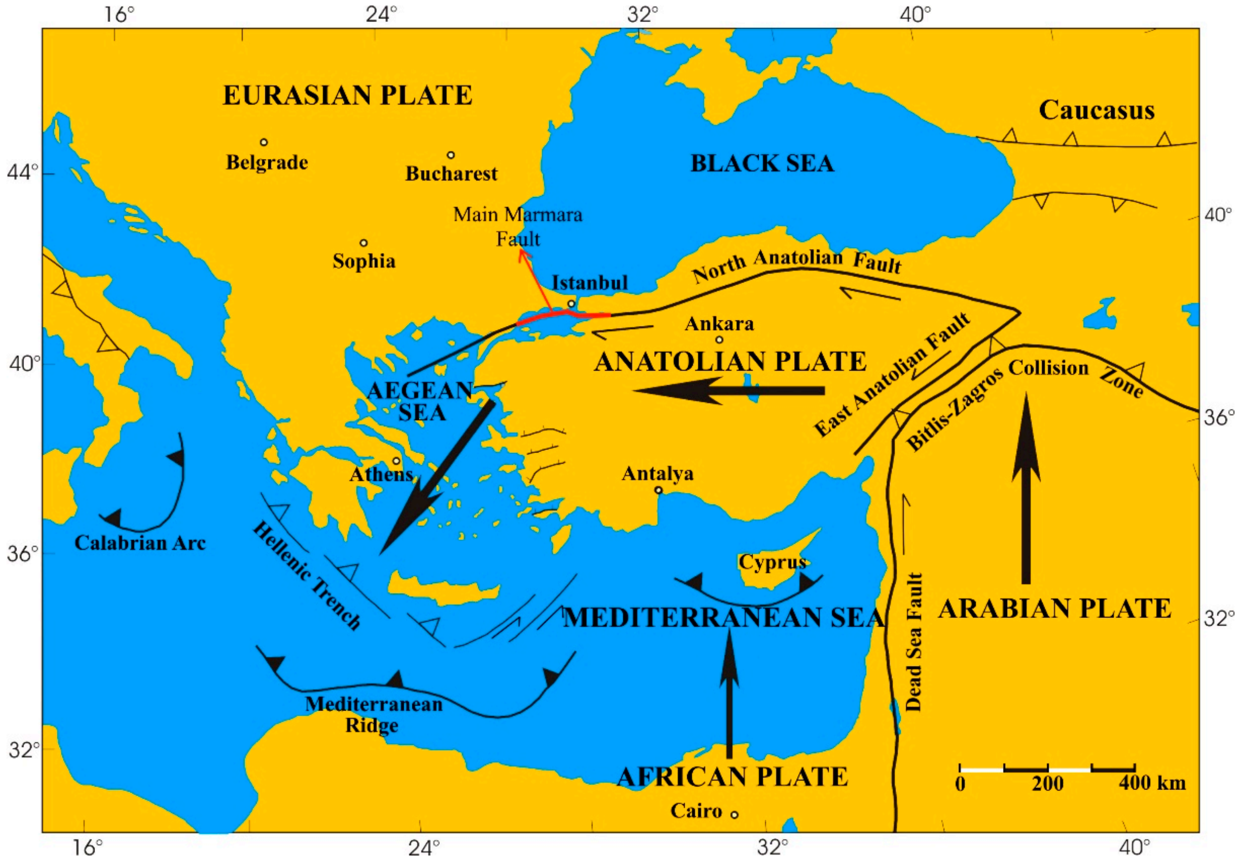


**Figure 1.** Anatolian plate tectonics (active thrust faults at continental collision zones are shown as lines with filled triangles, active subduction zones are indicated as lines with open triangles, normal faults are indicated as lines with unfilled triangles, and arrows indicate the motion of the plates) [3].

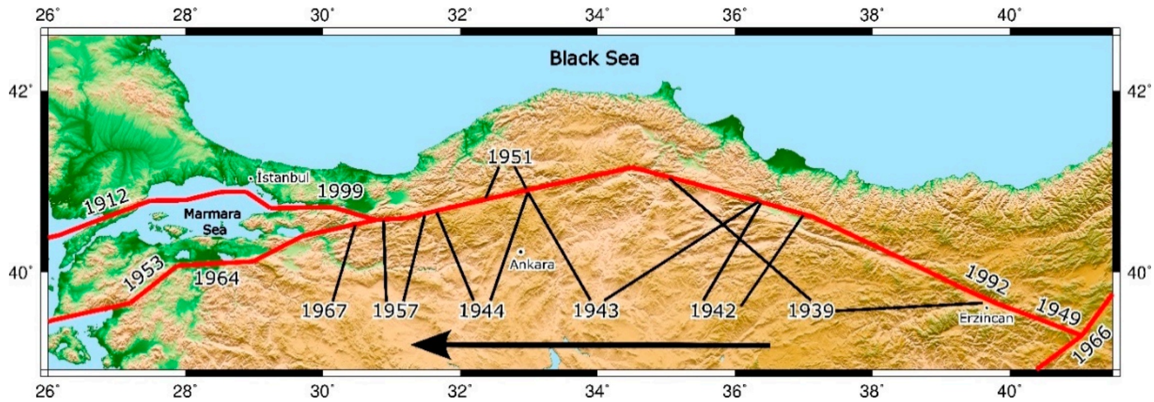


**Figure 2.** Earthquake sequence of the North Anatolian Fault (the arrow indicate the earthquake east to west migration).

Analytical methods whose mathematical equations are well defined can be solved directly and have definite results. Numerical methods are based on solving the defined problem iteratively through developing various approaches, and the results obtained are not definitive compared to those obtained through the analytical method. The results obtained through analytical methods offer great advantages because they are precise, accurate, and reliable. However, they have almost no applicability in complex problems [20]. Therefore, the use of numerical methods provides great advantages for complex, non-linear engineering problems that involve many variables.

In earth sciences, studies on determining deformation of the surface and interior parts of a homogeneous isotropic environment through elastic half-space modeling [21,22] can be cited as an example of the analytical method [23]. However, dislocation models ignore some physical phenomena such as frictional fault surfaces, and material structure and parameters. The results obtained from dislocation models can also be obtained using numerical modeling [23,24]. In addition, the dynamic approach can be used in numerical modeling.

Many of the physical phenomena discussed in the field of engineering can be explained through partial differential equations. It is almost impossible to solve these equations using analytical methods when solving models with arbitrary shapes [25]. The finite element method (FEM) is one of the numerical methods that enables these partial differential equations to be solved approximately. Unlike FEM, the solutions estimated with analytical methods are valid for that specific region and the results obtained are the same at every point of that region. FEM can be used for analyses such as stress, strain, fluid dynamics, etc.

The underwater part of the Main Marmara Fault has a more complex structure than other parts. Contrary to the fact that the fault in this section is stated to be a continuous and right-lateral slip fault [26], it is stated that it is discontinuous and has a pull-apart feature [27] (Figure 3). Also, this part is quite far from land. In other words, GNSS velocities cannot represent these fault movements well.

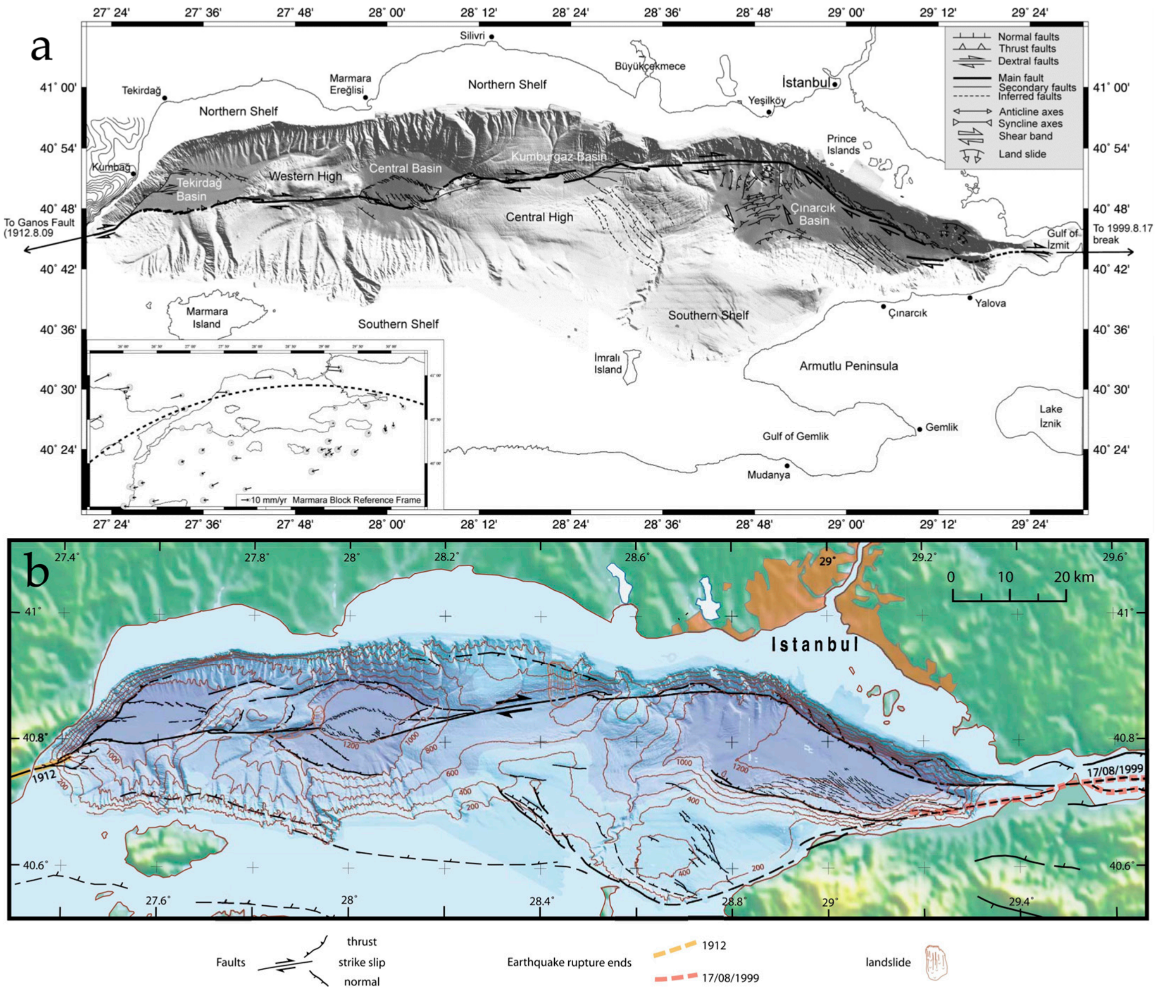


**Figure 3.** Active faults of Marmara Trough and bathymetric map: (**a**) the fault structure revealed by Le Pichon [26]; (**b**) the fault structure revealed by Armijo [27].

The magnitude of the possible earthquake rupture can be obtained using the slip deficits along the fault surfaces. Therefore, the accurate determination of the slip deficit to be achieved is logarithmically related to the magnitude of the possible seismic activity [28]. The finite element method (FEM), developed for the aviation industry in the 1950s [25,29], has recently been used in active tectonic studies [24,30–35]. Because, as mentioned, in addition to giving results close to the analytical methods, modeling can be performed through taking into account more complex structures and physical parameters using FEM. In this method, which discretizes the 3D model and solves the equations at the nodes according to the parameters, there has been no study on the effect of the mesh type on tectonic model results. In this study, in order to fill this gap in the literature, the MMF has been modeled using the FEM with different mesh types, and the accuracy of model results has been investigated.

## 2. Materials and Methods

It is stated that there are generally two types of analysis in solid mechanical analyses performed with the finite element method: static and dynamic [20]. Static analysis is a situation where the sum of the forces applied to the object is zero ($\Sigma F = 0$; F: force), that is, the internal and external forces applied to the system keep the object in balance. In this case, the system is considered independent of time. In dynamic analyses, the motion of the solid ($\Sigma F = ma$; m: mass, a: acceleration) is expressed with time-dependent functions. Because the system is not in balance, there is a movement. In this study, linear static analysis was carried out assuming that the sum of the forces applied to the system considered was zero.

In the finite element method, Equation (1) obtained for the entire system must be solved [25,36–38]. This is the global version of the equations written for each node. Here, F is the force, K is the global stiffness matrix, and U is the displacement.

$$F = K \times U \tag{1}$$

The stiffness matrix is obtained through the assembly of the equations written for each element created in FEM. Equation (2) shows the stiffness matrix of an element in the discretized model.

$$k_e = t \times A \times B^T \times D \times B \tag{2}$$

In this equation, t is the thickness of the element, A is the area, B is the strain–displacement matrix that converts the displacements at the nodes into strain, and D is the matrix that reveals the relationship between stress and strain [37]. When these equations written for each element are assembled, they form the global stiffness matrix (K) of the entire model. How the global stiffness matrix (K) is created can be explained with the system consisting of four linear springs in Figure 4.

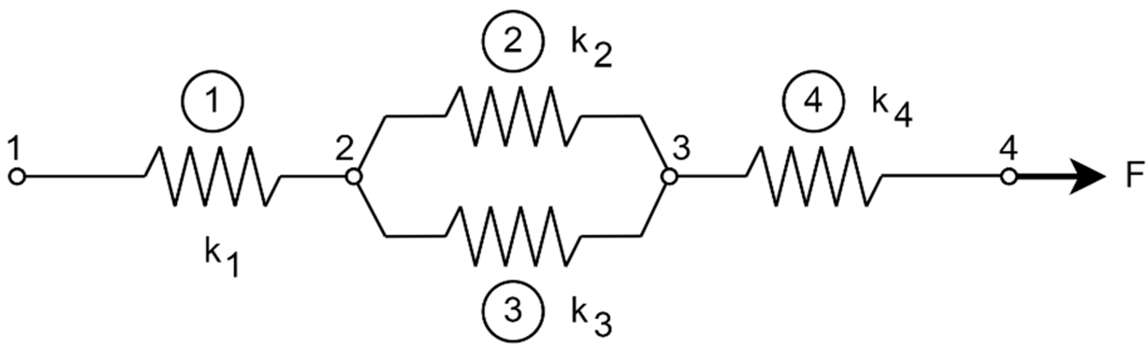


**Figure 4.** Linear springs system [36].

Each spring represents an element in the finite element method. The system consists of four nodes. Therefore, the stiffness matrix to be obtained will be $4 \times 4$ in size. A stiffness matrix for each element is written as in Equation (3).

$$
\begin{aligned}
\mathrm{k}_1 &= \begin{bmatrix} k_1^{11} & k_1^{12} & 0 & 0 \\ k_1^{21} & k_1^{22} & 0 & 0 \\ 0 & 0 & 0 & 0 \\ 0 & 0 & 0 & 0 \end{bmatrix} \\
\mathrm{k}_2 &= \begin{bmatrix} 0 & 0 & 0 & 0 \\ 0 & k_2^{22} & k_2^{23} & 0 \\ 0 & k_2^{32} & k_2^{33} & 0 \\ 0 & 0 & 0 & 0 \end{bmatrix} \\
\mathrm{k}_3 &= \begin{bmatrix} 0 & 0 & 0 & 0 \\ 0 & k_3^{22} & k_3^{23} & 0 \\ 0 & k_3^{32} & k_3^{33} & 0 \\ 0 & 0 & 0 & 0 \end{bmatrix} \\
\mathrm{k}_4 &= \begin{bmatrix} 0 & 0 & 0 & 0 \\ 0 & 0 & 0 & 0 \\ 0 & 0 & k_4^{33} & k_4^{34} \\ 0 & 0 & k_4^{43} & k_4^{44} \end{bmatrix}
\end{aligned} \tag{3}
$$

Here, the superscript refers to the number of nodes in each element of the matrix, and the subscript refers to the element number. There is a $k_1^{11} = k_1^{22} = k1$ and $k_1^{12} = k_1^{21} = -k_1$ relationship between the values in the stiffness matrix of each element. Through combining the stiffness matrices, the global stiffness matrix is obtained.

$$
\mathrm{K} = \mathrm{k}_1 + \mathrm{k}_2 + \mathrm{k}_3 + \mathrm{k}_4 \tag{4}
$$

The global stiffness matrix of this system, which consists of four one-dimensional springs, is formed as in Equation (5).

$$
\mathrm{K} = \begin{bmatrix} k_1^{11} & k_1^{12} & 0 & 0 \\ k_1^{21} & \left(k_1^{22} + k_2^{22} + k_3^{22}\right) & \left(k_2^{23} + k_3^{23}\right) & 0 \\ 0 & \left(k_2^{32} + k_3^{32}\right) & \left(k_2^{33} + k_3^{33} + k_4^{33}\right) & k_4^{34} \\ 0 & 0 & k_4^{43} & k_4^{44} \end{bmatrix} \tag{5}
$$

For finite element modeling studies, the first step is to create a 3D model. Parameters such as density, Poisson's ratio, and Young's modulus of the structure or material under consideration should be determined. The created geometry must be discretized into finite elements according to the selected element type. Finally, the system is solved through defining boundary conditions (Figure 5). For this study, the static structural module of ANSYS 2021 R1 academic software was used.

The fault geometry from the Reilinger [39] study has been used to create the 3D geometry to be used in the FEM modeling. The topography of the study area has been derived from the ETOPO1 model [40]. The depth of the 3D model has been set to the MOHO discontinuity depth. In addition, the model is created from three different layers in the vertical direction: upper crust, middle crust, and lower crust. The crusts and MOHO discontinuity depth values of the study area have been obtained from the Litho1.0 model [41]. The model boundaries have been chosen according to the distribution of GNSS stations located in the region [42], and Figure 6 map boundaries represent the 3D model edges.

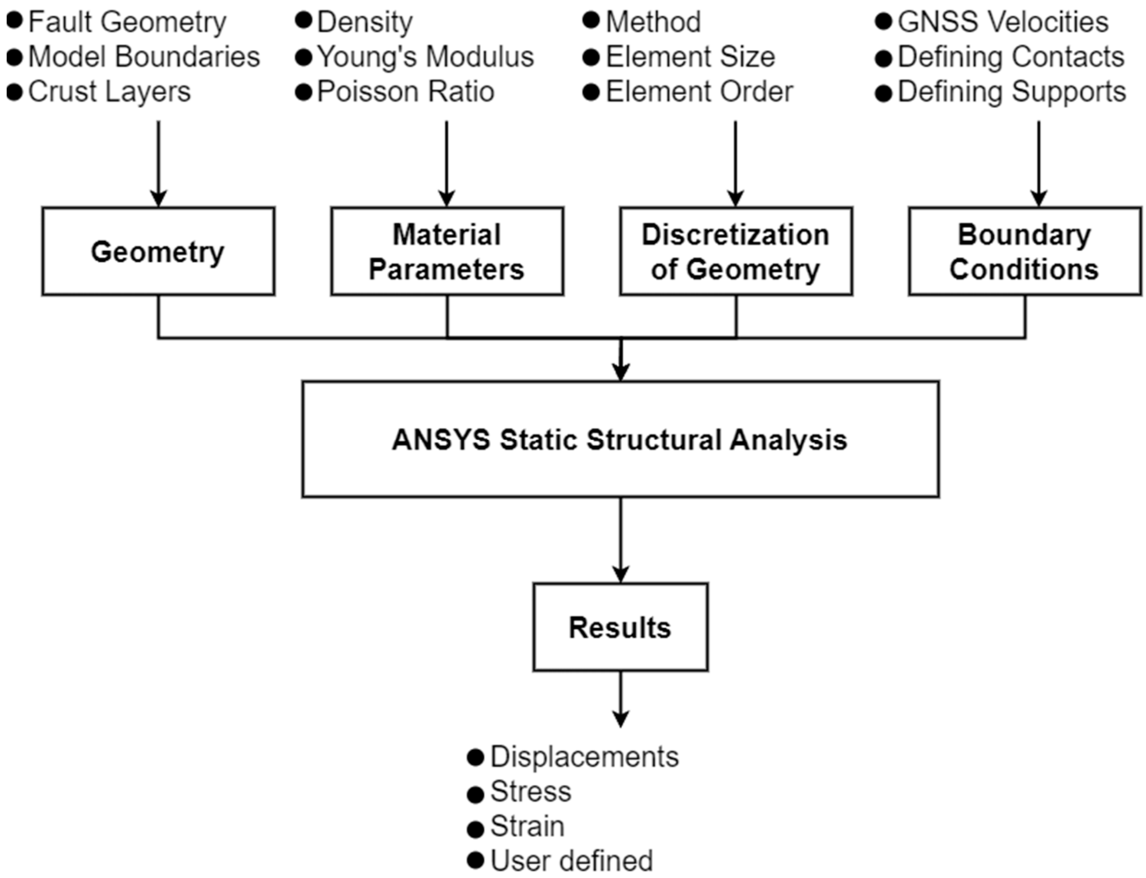


**Figure 5.** Processing inputs for the FEM model.

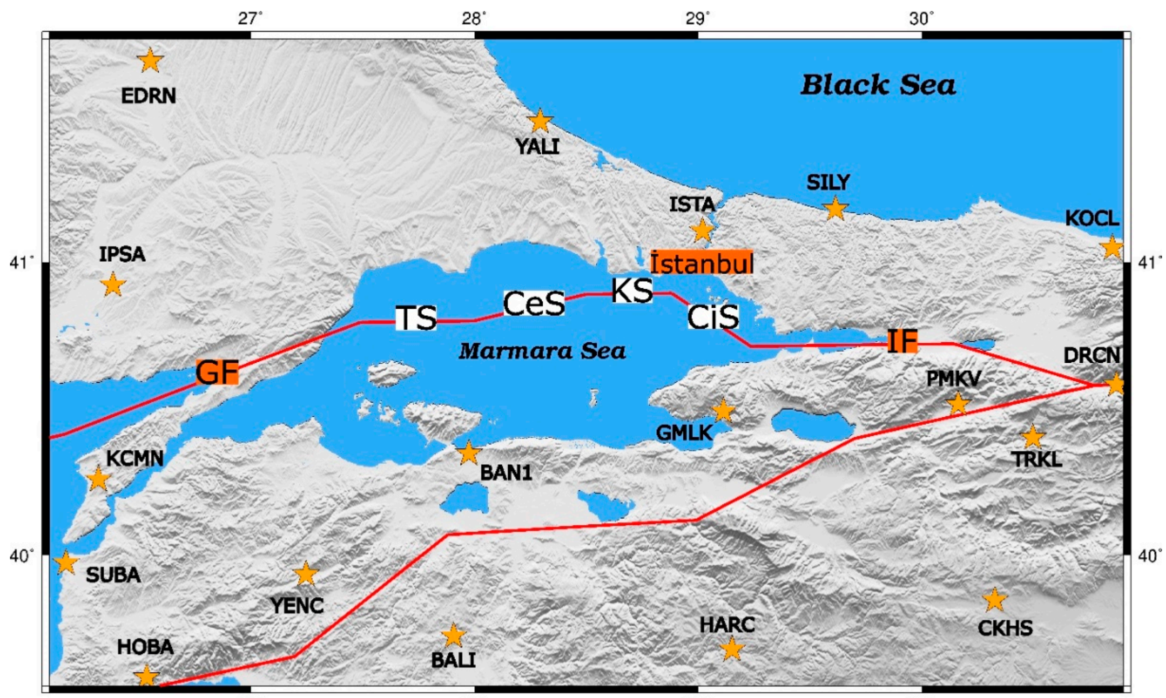


**Figure 6.** Main Marmara Fault and GNSS stations used for FEM modelling (GF: Ganos Fault, TS: Tekirdağ Segment, CeS: Central Segment, KS: Kumburgaz Segment, CiS: Çınarcık Segment, IF: İzmit Fault. Left bottom corner coordinates: latitude: 26°.10, longitude: 39°.20. Upper right corner coordinates: latitude: 30°.90, longitude: 41°.75).

The Poisson's ratio and Young's modulus have been calculated from velocities of P and S seismic waves that have been obtained from the Litho1.0 model [41] using Equations (6)–(9), and the density values have been obtained from the model directly. First, the Lamé parameters have to be calculated using the following formulae:

$$\mu = V_S^2 \times \rho \quad (6)$$

$$\lambda = V_P^2 \times \rho - 2 \times V_S^2 \times \rho \quad (7)$$

where μ is the shear or rigidity modulus, λ is the Lamé's first parameter [43,44], ρ is the density, and $V_P$ and $V_S$ are the seismic velocities. Then, the values of Young's modulus (E) and Poisson's ratio (ν) to be used for material identification can be calculated using Equations (3) and (4) [45,46].

$$E = \mu \times (3\lambda + 2\mu)/(\lambda + \mu) \quad (8)$$

$$\nu = \lambda/(2 \times (\lambda + \mu)) \quad (9)$$

In fact, since the same parameters have been used in all scenarios, any value in the literature could be used as a material parameter. The material parameters used in the study are given in Table 1.

**Table 1.** Material properties of crust layers (E and ν calculated using Equations (6)–(9); the other parameters were revealed from the Litho 1.0 model [41]).

| | Mean Depth (m) | Density (kg/m$^3$) | $V_P$ (m/s) | $V_s$ (m/s) | E (GPa) | ν |
|---|---|---|---|---|---|---|
| Upper Crust | | | | | | |
| Northern Part | 14,884 | 2783.202 | 6171.798 | 3595.387 | 89.452 | 0.243 |
| Middle Part | | 2755.755 | 6130.727 | 3568.524 | 87.296 | 0.244 |
| Southern Part | | 2673.685 | 5951.101 | 3463.532 | 79.792 | 0.244 |
| Middle Crust | | | | | | |
| Northern Part | 25,783 | 2870.239 | 6560.122 | 3789.549 | 103.013 | 0.250 |
| Middle Part | | 2806.795 | 6374.402 | 3690.362 | 95.405 | 0.248 |
| Southern Part | | 2737.393 | 6239.372 | 3607.668 | 88.990 | 0.249 |
| Lower Crust | | | | | | |
| Northern Part | 35,581 | 2991.605 | 7000.578 | 3899.408 | 116.004 | 0.275 |
| Middle Part | | 2894.723 | 6703.498 | 3676.326 | 100.542 | 0.285 |
| Southern Part | | 2833.714 | 6626.517 | 3692.061 | 98.492 | 0.275 |

Frictional contact has been defined between fault surfaces. In studies conducted in the literature, friction coefficients in the range of 0.02–0.05 were used for the North Anatolian Fault [32,47–49]. It has been stated that the values used in this range give the best model results. The friction coefficient has been chosen to be 0.05.

Three-dimensional geometry was created using the fault geometry used in the Reilinger [39] study, determined model boundaries, crustal layers, and topography. The visual appearance of this created 3D geometry in ANSYS software is given in Figure 7.

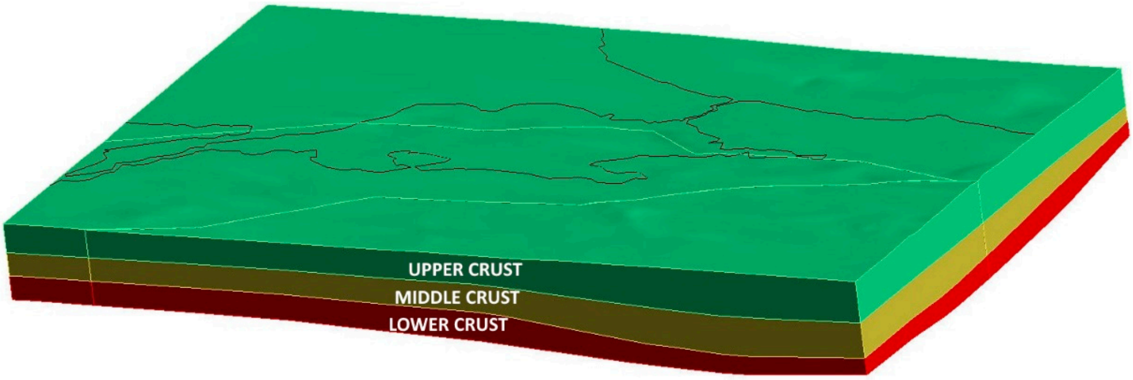


**Figure 7.** Created 3D geometry of the study area.

In order to discretize the created geometry, the element size, the element order, and the method was chosen as 4000 m, quadratic, and *patch conforming,* respectively.It is stated that discretizing the model into smaller elements will increase model accuracy [25], but this will increase the processing time and no solution may be obtained depending on the capacity of the computer. The 4000 m value was chosen here because the distance where the GNSS stations are closest to each other is approximately 4 km. There are two different options for element ordering in ANSYS software. These are linear and quadratic. Irregular shapes can be represented better with quadratic order. The surfaces of the geometry obtained in this study are not linear. Therefore, quadratic order was preferred. ANSYS software offers two methods for discretizing the model: patch conforming (bottom-up approach) or patch independent (top-down approach). These are the methods that specify how the mesh operation will be performed. In the patch-conforming method, the discretization process is carried out starting from the edges and moving towards the interior of the model. Thus, the boundaries of the model are preserved. The patch-independent method is vice versa, and the mesh process is performed from the inside to the outside of the model.

After the mesh process, the elements and the nodes connecting them are formed. The value of the annual GNSS velocities at the nodes corresponding to the GNSS stations in the mesh network formed on the surface is defined as displacement. In total 18 GNSS station (Figure 6) velocities [42] have been defined as displacement in the software. The east, west, and north of the northern part of the MMF and the bottom surface of the entire 3D model have been selected as supports (Figure 8). The other GNSS station velocities that are in the study area have been used as test stations, and Root Mean Square Error (RMSE) values have been calculated through comparing GNSS and model velocities using Equation (10). This allows quantitative comparisons to be made between the model results.

$$\mathrm{RMSE} = \sqrt{\frac{\sum_{i=1}^{n} \left(v_{GNSS,i} - v_{model,i}\right)^2}{n}} \tag{10}$$

Here $v_{GNSS}$ and $v_{model}$ are the velocities of the GNSS stations and the model, respectively.

There are many different meshing methods in ANSYS software. These are called *tetrahedron*, *hex dominant*, *sweep*, *multizone*, *cartesian*, and *layered tetrahedron*. The element types used in the meshing are given in Figure 9. The methods use these elements.

The *tetrahedron* method uses only tetrahedron elements. In the *hex-dominant* method, the hexahedron element is mainly used. It is recommended to use it in geometries that cannot be swept. In the *sweep* method, if the object has a structure that can be swept, meshing is performed using hexahedron and prism elements. When this method is selected, it is also possible to define how the surfaces are meshed. When *quad/tri* is selected, triangle and quadrilateral 2D elements are used together. In the *all tri* and *all quad* options, completely triangle and quadrilateral elements are used, respectively. In the *multizone* method, discretization is performed according to the mapped mesh type selected. These options specify whether only hexahedron, or only prism, or both are used. In the software, they are named *hexa*, *prism,* and *hex/prism,* respectively. The *cartesian* methods fits the geometry with an unstructured, relatively uniformly sized hexahedron element that is aligned to the given coordinate system. The *layered tetrahedrons* mesh approach fits the geometry through layering an unstructured tetrahedron element on a given layer height.

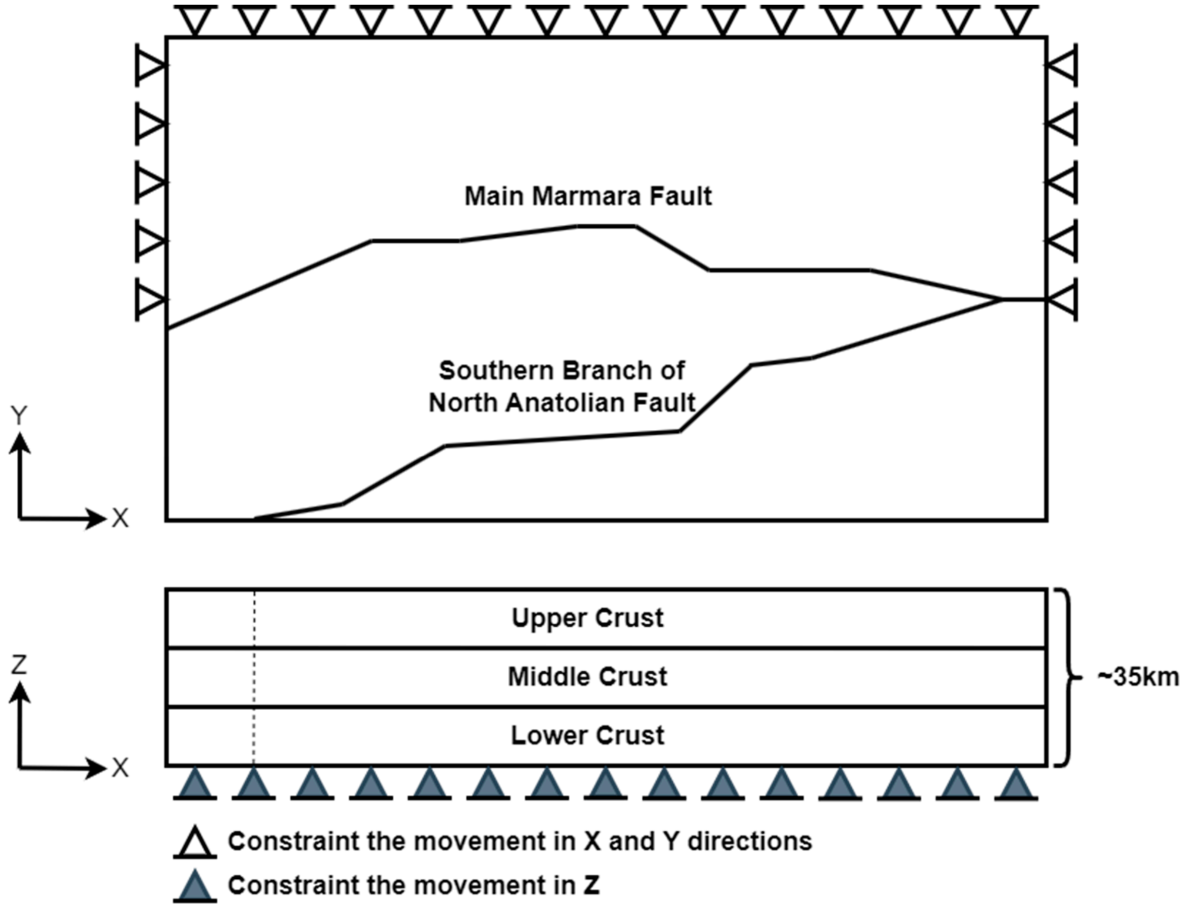


**Figure 8.** Supports defined in ANSYS software.

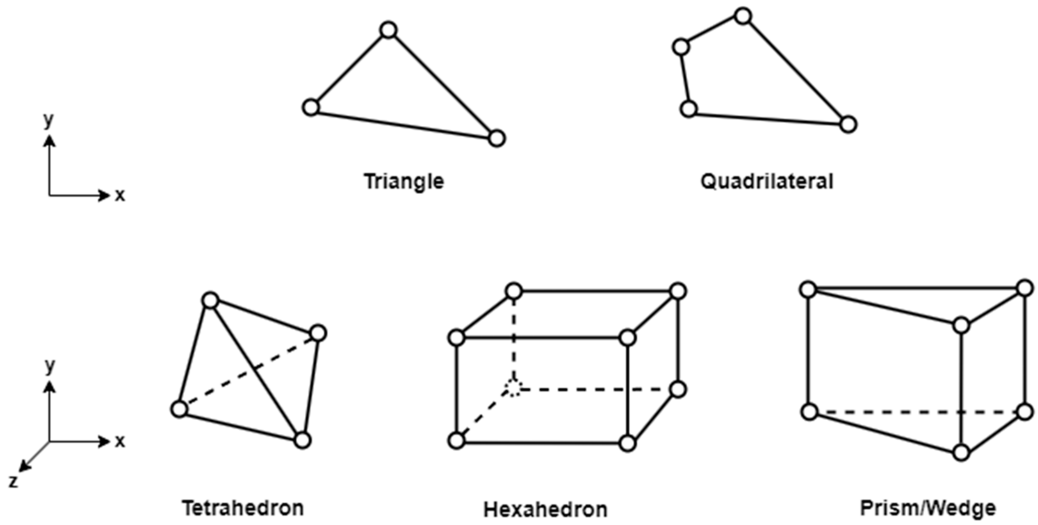


**Figure 9.** Mesh types (triangle and quadrilateral are 2D and the others are 3D).

To summarize, the fault geometry used in the Reilinger [39] study, the velocities of the 18 GNSS stations obtained in the Kurt [42] study for the displacement boundary condition, the elasticity parameters calculated from the seismic velocities, and the density revealed from Litho 1.0 model. The friction coefficient of contact surfaces was set as 0.05. The supports of the geometry were applied to the FEM model as shown in Figure 8.

In this study, the 3D geometry has been discretized using the methods available in the software. All parameters used in the model (material properties, friction coefficient, supports, displacements, etc.) have not been changed except the mesh type. Therefore, only the effect of the mesh type on the accuracy of the model can be revealed.

## 3. Results

In order to investigate the accuracy of the tectonic models using different mesh types in ANSYS software, *tetrahedron*, *sweep*, and *multizone* mesh methods have been used. The 3D geometry could not be discretized using the *hex-dominant* and *layered tetrahedron* mesh methods. Although discretizing could be performed using the *cartesian method*, the model result could not be obtained due to the distorted geometry formed on the contact surfaces in the static structural analysis. Therefore, the model results have been obtained using *tetrahedron*, *sweep*, and *multizone* mesh methods.

In the sweep method, there are *quad/tri*, *all tri*, and *all quad* options in the *free mesh type* section. Of these, *quad/tri* and *all tri* have been used. Although *all quad* has been selected, some elements were created as *tri*, therefore, this method is considered unnecessary for analysis. In the *multizone* method, there are the *hex/prism*, *hexa*, and *prism* options under mapped mesh type. The analysis could be performed using all of these options. In order to reveal the effect of the mesh type on the results, all inputs have not been changed except for the mesh type in all scenarios. As a result, the RMSE values have been calculated using Equation (10) and are given in Table 2.

**Table 2.** RMSE of different mesh type scenarios.

| Mesh Type | Face Mesh Type | Mapped Mesh Type | Number of Nodes | East RMSE (mm) | North RMSE (mm) |
|---|---|---|---|---|---|
| Tetrahedron | - | - | 487,279 | 1.53 | 1.09 |
| Sweep | Quad/Tri | - | 407,106 | 1.61 | 1.11 |
| Sweep | All Tri | - | 516,457 | 1.57 | 1.11 |
| Multizone | - | Hexa/Prism | 452,636 | 1.60 | 1.14 |
| Multizone | - | Hexa | 457,776 | 1.61 | 1.13 |
| Multizone | - | Prism | 614,995 | 1.65 | 1.12 |

According to the RMSE values, the best result has been obtained with the *tetrahedron* mesh method. The mesh method with the lowest accuracy is the *multizone with prism mapped mesh type*. However, the difference between them is only one tenth of a millimeter. In order to reveal the effect of these differences on the earthquake magnitude to be calculated, slip deficit values on the fault have been calculated for one year. Considering that seismic gapin this region is about 250 years [5,12,16,18,50–53], in order to calculate the magnitude of the earthquake, the total slip deficit should be calculated through multiplying the annual slip deficit by 250. The a and b coefficients and equation given in the study by Wells [28] have been used to reveal the possible rupture magnitude (Equation (11)).

$$M_w = a + b \times \log(MD) \tag{11}$$

The a and b coefficients were obtained as a result of the regression analysis between the moment magnitudes ($M_w$) of the earthquakes and the resulting displacement (MD in meters). The coefficients were obtained as 6.81 and 0.78, respectively, for strike-slip faults. Equation (11) gives the relationship between earthquake magnitudes and observed displacements after the earthquakes. This equation can be used to calculate the moment magnitude of possible earthquakes. Here, instead of displacement, the slip deficit obtained as a result of the model analysis was used.

These magnitudes have only been calculated for the *tetrahedron* and *multizone–prism* methods, which have the lowest and highest east RMSE values, respectively. According to the model results, two fault zones have high strain values. One of them is GF and the other is the intersection of IF and CiS. The annual slip deficit value in GF was the same in the results obtained from both mesh types. At the intersection of IF and CiS, the difference in the slip deficit values obtained is approximately 0.5 mm. In Equation (11), there is a logarithmic equation between moment magnitude and displacement. Accordingly, if the annual slip deficit is considered to occur between 0 and 25 mm, the graph of the difference values caused by the 0.5 mm difference in the moment magnitude calculation is obtained (Figure 10). If the slip deficit occurs between 9 and 25 mm per year, the magnitude is 0.01, if it is between 7 and 8 mm, the magnitude difference is 0.02, if it is between 5 and 6 mm, the magnitude difference is 0.03, and for an annual slip deficit of 0–4, the magnitude difference varies between 0.04 and 0.14.

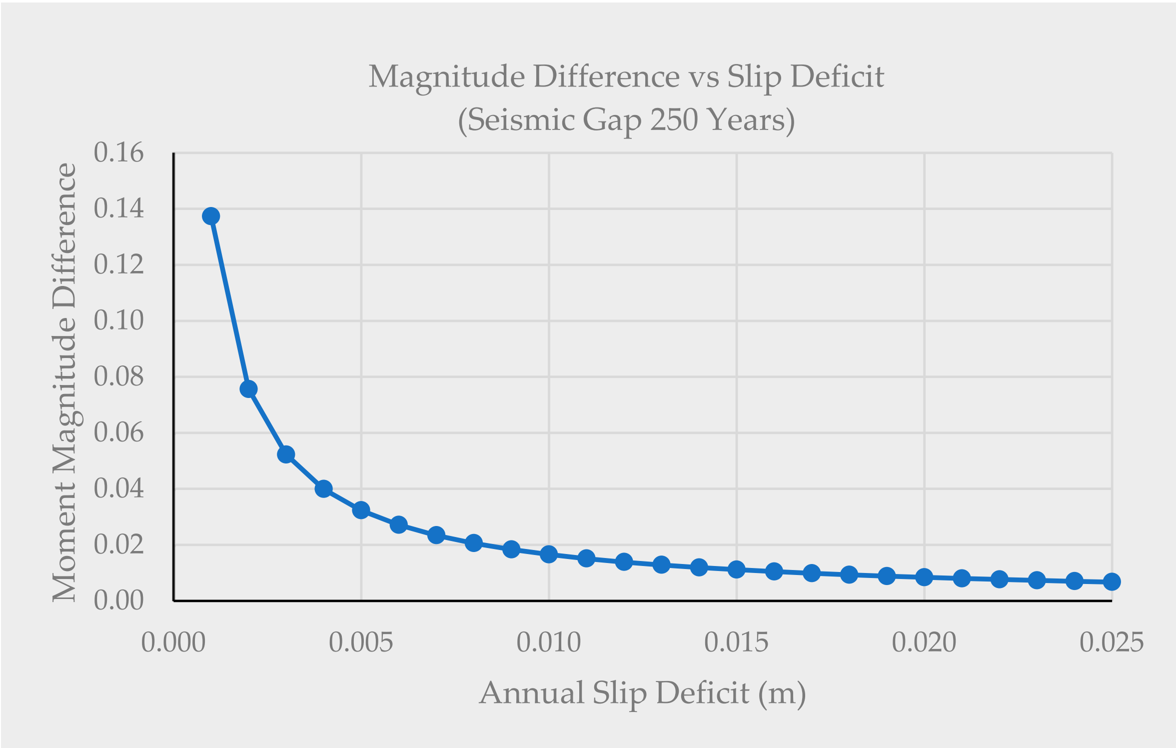


**Figure 10.** Magnitude difference for 0.5 mm annual slip deficit difference of *tetrahedron* and *multizone–prism* mesh types.

Using the moment magnitude value, the amount of energy that will be released during an earthquake rupture can be calculated using Equation (12) [54].

$$\log E = 5.24 + 1.44 \times M_w \tag{12}$$

Here, $M_w$ represents the moment magnitude and E represents the energy released during the earthquake. The unit of the calculated energy amount is Joule.

Figure 10 shows the graph of the change in moment magnitude calculated according to different slip deficits. Using Equation (12), the graph of the change in energy release that will occur with possible fracture according to different slip deficits is given in Figure 11.

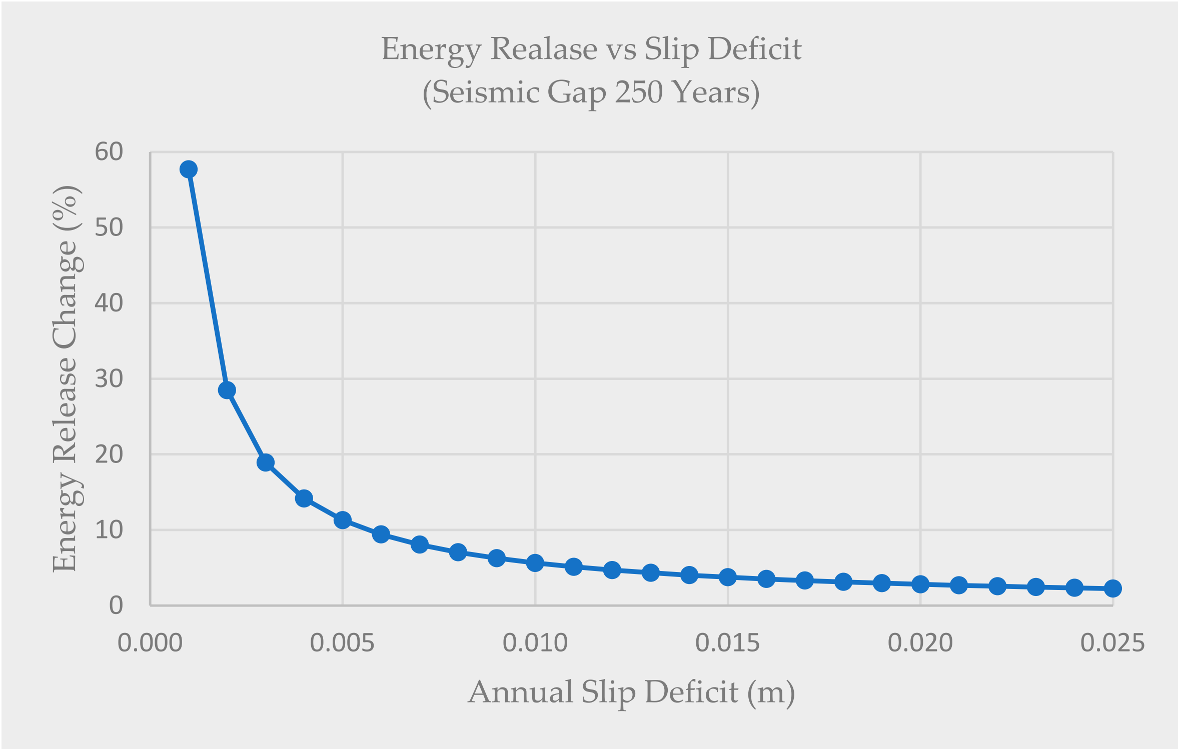


**Figure 11.** Energy release change for 0.5 mm annual slip deficit difference of *tetrahedron* and *multizone–prism* mesh types.

## 4. Discussion

Earthquakes cause loss of life and property depending on their magnitude. The probability of an earthquake rupture and magnitude in a region can be determined through the region's seismic cycles and the slip deficits of the fault surfaces. The slip deficits on the fault surfaces cannot be determined directly but can be estimated using analytical and numerical modeling techniques. FEM is one such powerful numerical modeling technique to simulate complex engineering problems. This method is based on the principle of discretizing the generated geometry into elements that connected to each other with nodes and solving the equations at the nodes. Estimating the location and magnitude of possible earthquakes is directly related to the accuracy of the parameters used in the created model. In interseismic tectonic studies, it is very important to accurately determine the slip deficits of the fault surfaces, especially in revealing the possible rupture magnitude.

Elements with different structures are used in the discretization of the geometry created in studies using FEM. When we examine the studies in the literature [24,30–35], there is no study that has been conducted on the effect of different mesh types on model results. In this study, it has been observed that the meshing performed with the tetrahedron method that uses the *tetrahedron* element type gives better results on the Main Marmara Fault. When the annual slip deficit values on the fault surfaces of the GF and IF–CiS intersections were compared in the scenarios, there is no difference between the slip deficit rates on the GF surface. At the IF–CiS intersection, an annual difference of 0.5 mm was obtained. Depending on slip deficit and the seismic gap value, the moment magnitude difference values vary between 0.04 and 0.14. As the moment magnitude increases, the amount of energy released increases logarithmically. As a result of two different scenarios, there is a change between 60% and 2% in the calculated energy release. This corresponds to the energy range of $1 \times 10^{14}$ to $2 \times 10^{14}$ joules. If the total slip deficit is large, the difference in energy release is almost twice as much in terms of energy release, even though its percentage difference is low. In other words, although the difference in the annual slip deficit value obtained between the scenarios is small, the calculated energy release values can reach serious levels. Therefore, the *tetrahedron* element should be preferred in analyses to be performed with FEM.

These results have been revealed using ANSYS software. Apart from ANSYS, there are many other powerful FEM software used in tectonic modeling studies. In future studies, the effect of mesh type can be investigated in different FEM software. Additionally, the results have been revealed using a study area. Therefore, similar studies should be applied to different study areas and different fault types.

## 5. Conclusions

The studies in the literature examining seismic potential with the finite element method have not yet revealed the effect of element types used in the model's discretization on the model and fault surface slip deficit. In order to fill this gap in the literature, the Main Marmara Fault, located in the Marmara region of the North Anatolian Fault, where an earthquake of magnitude seven or higher is expected, was modeled. Three-dimensional geometry was used in the modeling study. To obtain the 3D geometry, the area with left corner coordinates latitude: 26°.10, longitude: 39°.20, and upper right coordinates latitude: 30°.90, longitude: 41°.75 was created. The fault geometry used in the Reilinger [39] study within this area was used. Three-dimensional geometry is considered as three vertical layers: upper, middle, and lower crust, and topography is added. Material parameters were obtained from the Litho 1.0 model, and the friction coefficient along the fault surfaces was entered as 0.05. The annual velocities of the 18 GNSS stations obtained in the Kurt [42] study were manipulated as displacements in the software. Supports were applied to the surfaces of the parts north of the Main Marmara Fault and from the bottom of the model. The created model was solved using different mesh methods in ANSYS software. According to the RMSE values calculated through comparing the GNSS test stations with the values obtained from the model, the *tetrahedron* method obtained the best results with 1.53 and 1.09, and the *multizone–prism* method obtained the worst results with 1.65 and 1.12 east and west RMSE components, respectively.

As a result of the comparison between the best and worst models on the fault surfaces, the slip deficits at the GF and IF–CiS intersection, which have large slip deficit values, were compared. As a result of this comparison, GF slip deficit values are the same, but the IF–CiS intersection has a 0.5 mm difference. For the *multizone–prism* mesh method, the annual slip deficit has been calculated to be less than the *tetrahedron* method.

**Author Contributions:** Conceptualization, M.F.K.; methodology, M.F.K.; software, M.F.K.; validation, M.F.K.; formal analysis, M.F.K.; investigation, M.F.K.; resources, M.F.K.; data curation, M.F.K.; writing—original draft preparation, M.F.K.; writing—review and editing, M.F.K. and V.E.G.; visualization, M.F.K.; supervision, V.E.G.; project administration, M.F.K. All authors have read and agreed to the published version of the manuscript.

**Funding:** This research received no external funding.

**Institutional Review Board Statement:** Not applicable.

**Informed Consent Statement:** Not applicable.

**Data Availability Statement:** The data that support the findings of this study are available from the corresponding author, upon reasonable request. The data are not publicly available due to privacy.

**Conflicts of Interest:** The authors declare no conflict of interest.

## References

1. Bird, P. An updated digital model of plate boundaries. *Geochem. Geophys. Geosystems* **2003**, *4*, 1–52. [CrossRef]
2. McKenzie, D. Active tectonics of the Mediterranean region. *Geophys. J. Int.* **1972**, *30*, 109–185. [CrossRef]
3. Okay, A.İ.; Kaşlılar-Özcan, A.; İmren, C.; Boztepe-Güney, A.; Demirbağ, E.; Kuşçu, İ. Active faults and evolving strike-slip basins in the Marmara Sea, northwest Turkey: A multichannel seismic reflection study. *Tectonophysics* **2000**, *321*, 189–218. [CrossRef]
4. Şengör, A.; Tüysüz, O.; Imren, C.; Sakınç, M.; Eyidoğan, H.; Görür, N.; Le Pichon, X.; Rangin, C. The North Anatolian fault: A new look. *Annu. Rev. Earth Planet. Sci.* **2005**, *33*, 37–112. [CrossRef]

5. Ambraseys, N. The seismic activity of the Marmara Sea region over the last 2000 years. *Bull. Seismol. Soc. Am.* **2002**, *92*, 1–18. [CrossRef]
6. Stein, R.S.; Barka, A.A.; Dieterich, J.H. Progressive failure on the North Anatolian fault since 1939 by earthquake stress triggering. *Geophys. J. Int.* **1997**, *128*, 594–604. [CrossRef]
7. Tiryakioğlu, İ.; Aktuğ, B.; Yiğit, C.; Yavaşoğlu, H.; Sözbilir, H.; Özkaymak, Ç.; Poyraz, F.; Taneli, E.; Bulut, F.; Doğru, A. Slip distribution and source parameters of the 20 July 2017 Bodrum-Kos earthquake (Mw6. 6) from GPS observations. *Geodinamica acta* **2018**, *30*, 1–14. [CrossRef]
8. Özarpacı, S.; Doğan, U.; Ergintav, S.; Çakır, Z.; Özdemir, A.; Floyd, M.; Reilinger, R. Present GPS velocity field along 1999 Izmit rupture zone: Evidence for continuing afterslip 20 yr after the earthquake. *Geophys. J. Int.* **2020**, *224*, 2016–2027. [CrossRef]
9. Straub, C.; Kahle, H.-G. Global Positioning System (GPS) estimates of crustal deformation in the Marmara Sea region, Northwestern Anatolia. *Earth Planet. Sci. Lett.* **1994**, *121*, 495–502. [CrossRef]
10. Straub, C.; Kahle, H.G.; Schindler, C. GPS and geologic estimates of the tectonic activity in the Marmara Sea region, NW Anatolia. *J. Geophys. Res. Solid Earth* **1997**, *102*, 27587–27601. [CrossRef]
11. Tiryakioğlu, İ.; Floyd, M.; Erdoğan, S.; Gülal, E.; Ergintav, S.; McClusky, S.; Reilinger, R. GPS constraints on active deformation in the Isparta Angle region of SW Turkey. *Geophys. J. Int.* **2013**, *195*, 1455–1463. [CrossRef]
12. Yavasoglu, H.; Tiryakioglu, I.; Karabulut, M.; Eyubagil, E.; Ozkan, A.; Masson, F.; Klein, E.; Gulal, V.; Alkan, R.; Alkan, M. New geodetic constraints to reveal seismic potential of central Marmara region, Turkey. *Boll. Geofis. Teor. Appl.* **2021**, *62*, 513–526.
13. Barka, A.; Akyuz, H.; Altunel, E.; Sunal, G.; Cakir, Z.; Dikbas, A.; Yerli, B.; Armijo, R.; Meyer, B.; De Chabalier, J. The surface rupture and slip distribution of the 17 August 1999 Izmit earthquake (M 7.4), North Anatolian fault. *Bull. Seismol. Soc. Am.* **2002**, *92*, 43–60. [CrossRef]
14. Toksöz, M.; Shakal, A.; Michael, A. Space-time migration of earthquakes along the North Anatolian fault zone and seismic gaps. *Pure Appl. Geophys.* **1979**, *117*, 1258–1270. [CrossRef]
15. Bohnhoff, M.; Bulut, F.; Dresen, G.; Malin, P.E.; Eken, T.; Aktar, M. An earthquake gap south of Istanbul. *Nat. Commun.* **2013**, *4*, 1999. [CrossRef] [PubMed]
16. Ergintav, S.; Reilinger, R.; Çakmak, R.; Floyd, M.; Cakir, Z.; Doğan, U.; King, R.; McClusky, S.; Özener, H. Istanbul's earthquake hot spots: Geodetic constraints on strain accumulation along faults in the Marmara seismic gap. *Geophys. Res. Lett.* **2014**, *41*, 5783–5788. [CrossRef]
17. Hubert-Ferrari, A.; Barka, A.; Jacques, E.; Nalbant, S.S.; Meyer, B.; Armijo, R.; Tapponnier, P.; King, G.C. Seismic hazard in the Marmara Sea region following the 17 August 1999 Izmit earthquake. *Nature* **2000**, *404*, 269–273. [CrossRef]
18. Klein, E.; Duputel, Z.; Masson, F.; Yavasoglu, H.; Agram, P. Aseismic slip and seismogenic coupling in the Marmara Sea: What can we learn from onland geodesy? *Geophys. Res. Lett.* **2017**, *44*, 3100–3108. [CrossRef]
19. Schmittbuhl, J.; Karabulut, H.; Lengliné, O.; Bouchon, M. Seismicity distribution and locking depth along the M ain M armara F ault, T urkey. *Geochem. Geophys. Geosystems* **2016**, *17*, 954–965. [CrossRef]
20. Bower, A.F. *Applied Mechanics of Solids*; CRC Press: Boca Raton, CA, USA, 2009.
21. Okada, Y. Surface deformation due to shear and tensile faults in a half-space. *Bull. Seismol. Soc. Am.* **1985**, *75*, 1135–1154. [CrossRef]
22. Okada, Y. Internal deformation due to shear and tensile faults in a half-space. *Bull. Seismol. Soc. Am.* **1992**, *82*, 1018–1040. [CrossRef]
23. Pasupuleti, V.D.K. Non-Linear Numerical Modeling of Tectonic Plate for Understanding Crustal Deformation and Stress Accumulation at Plate Junctions. Ph.D. Thesis, International Institute of Information Technology, Hyderabad, India, 2016.
24. Masterlark, T. Finite element model predictions of static deformation from dislocation sources in a subduction zone: Sensitivities to homogeneous, isotropic, Poisson-solid, and half-space assumptions. *J. Geophys. Res. Solid Earth* **2003**, *108*. [CrossRef]
25. Belytschko, T.; Fish, J. *A First Course in Finite Elements*; John Wiley & Sons Ltd.: Chichester, UK, 2007.
26. Le Pichon, X.; Şengör, A.; Demirbağ, E.; Rangin, C.; Imren, C.; Armijo, R.; Görür, N.; Çağatay, N.; De Lepinay, B.M.; Meyer, B. The active main Marmara fault. *Earth Planet. Sci. Lett.* **2001**, *192*, 595–616. [CrossRef]
27. Armijo, R.; Meyer, B.; Navarro, S.; King, G.; Barka, A. Asymmetric slip partitioning in the Sea of Marmara pull-apart: A clue to propagation processes of the North Anatolian fault? *Terra Nova* **2002**, *14*, 80–86. [CrossRef]
28. Wells, D.L.; Coppersmith, K.J. New empirical relationships among magnitude, rupture length, rupture width, rupture area, and surface displacement. *Bull. Seismol. Soc. Am.* **1994**, *84*, 974–1002. [CrossRef]
29. Turner, M.J.; Clough, R.W.; Martin, H.C.; Topp, L. Stiffness and deflection analysis of complex structures. *J. Aeronaut. Sci.* **1956**, *23*, 805–823. [CrossRef]
30. Diao, F.; Wang, R.; Aochi, H.; Walter, T.R.; Zhang, Y.; Zheng, Y.; Xiong, X. Rapid kinematic finite-fault inversion for an M w 7+ scenario earthquake in the Marmara Sea: An uncertainty study. *Geophys. J. Int.* **2016**, *204*, 813–824. [CrossRef]
31. Heidbach, O.; Drewes, H. 3D Finite element model of major tectonic processes in the Eastern Mediterranean. *Geol. Soc. Lond. Spec. Publ.* **2003**, *212*, 261–274. [CrossRef]
32. Hergert, T.; Heidbach, O.; Bécel, A.; Laigle, M. Geomechanical model of the Marmara Sea region—I. 3-D contemporary kinematics. *Geophys. J. Int.* **2011**, *185*, 1073–1089. [CrossRef]
33. Liu, M.; Yang, Y.; Li, Q.; Zhang, H. Parallel computing of multi-scale continental deformation in the Western United States: Preliminary results. *Phys. Earth Planet. Inter.* **2007**, *163*, 35–51. [CrossRef]

34. Oglesby, D.D.; Mai, P.M. Fault geometry, rupture dynamics and ground motion from potential earthquakes on the North Anatolian Fault under the Sea of Marmara. *Geophys. J. Int.* **2012**, *188*, 1071–1087. [CrossRef]
35. Parsons, T. Recalculated probability of M $\geq$ 7 earthquakes beneath the Sea of Marmara, Turkey. *J. Geophys. Res. Solid Earth* **2004**, *109*, 1–21. [CrossRef]
36. Madenci, E.; Guven, I. *The Finite Element Method and Applications in Engineering Using ANSYS®*; Springer: Berlin, Germany, 2015.
37. Ramsay, J.G.; Huber, M.I.; Lisle, R.J. *The Techniques of Modern Structural Geology: Applications of Continuum Mechanics in Structural Geology*; Elsevier: Amsterdam, The Netherlands, 2000; Volume 3.
38. Stephansson, O.; Berner, H. The finite element method in tectonic processes. *Phys. Earth Planet. Inter.* **1971**, *4*, 301–321. [CrossRef]
39. Reilinger, R.; McClusky, S.; Vernant, P.; Lawrence, S.; Ergintav, S.; Cakmak, R.; Ozener, H.; Kadirov, F.; Guliev, I.; Stepanyan, R. GPS constraints on continental deformation in the Africa—Arabia—Eurasia continental collision zone and implications for the dynamics of plate interactions. *J. Geophys. Res. Solid Earth* **2006**, *111*, 1–26. [CrossRef]
40. Amante, C.; Eakins, B.W. ETOPO1 Arc-Minute Global Relief Model: Procedures, Data Sources and Analysis. 2009. Available online: https://repository.library.noaa.gov/view/noaa/1163 (accessed on 5 July 2021).
41. Pasyanos, M.E.; Masters, T.G.; Laske, G.; Ma, Z. LITHO1. 0: An updated crust and lithospheric model of the Earth. *J. Geophys. Res. Solid Earth* **2014**, *119*, 2153–2173. [CrossRef]
42. Kurt, A.İ.; Öbakır, A.D.; Cingöz, A.; Eergintav, S.; Doğan, U.; Özarpacı, S. Contemporary velocity field for Turkey inferred from combination of a dense network of long term GNSS observations. *Turk. J. Earth Sci.* **2023**, *32*, 275–293. [CrossRef]
43. Goodway, B.; Chen, T.; Downton, J. Improved AVO fluid detection and lithology discrimination using Lamé petrophysical parameters;"λρ", "μρ", & "λ/μ fluid stack", from P and S inversions. In *SEG Technical Program Expanded Abstracts 1997*; Society of Exploration Geophysicists: Houston, TX, USA, 1997; pp. 183–186.
44. Mavko, G.; Mukerji, T.; Dvorkin, J. *The Rock Physics Handbook*; Cambridge University Press: Cambridge, UK, 2020.
45. Feng, K.; Shi, Z.-C. *Mathematical Theory of Elastic Structures*; Springer Science & Business Media: Berlin, Germany, 2013.
46. Salençon, J. *Handbook of Continuum Mechanics: General Concepts Thermoelasticity*; Springer Science & Business Media: Berlin, Germany, 2012.
47. Jiménez-Munt, I.; Sabadini, R. The block-like behavior of Anatolia envisaged in the modeled and geodetic strain rates. *Geophys. Res. Lett.* **2002**, *29*, 39-1–39-4. [CrossRef]
48. Provost, A.-S.; Chéry, J.; Hassani, R. 3D mechanical modeling of the GPS velocity field along the North Anatolian fault. *Earth Planet. Sci. Lett.* **2003**, *209*, 361–377. [CrossRef]
49. Vernant, P.; Chery, J. Low fault friction in Iran implies localized deformation for the Arabia–Eurasia collision zone. *Earth Planet. Sci. Lett.* **2006**, *246*, 197–206. [CrossRef]
50. Ambraseys, N.; Finkel, C. Long-term seismicity of Istanbul and of the Marmara Sea region. *Terra Nova* **1991**, *3*, 527–539. [CrossRef]
51. Ambraseys, N.N.; Jackson, J. Seismicity of the Sea of Marmara (Turkey) since 1500. *Geophys. J. Int.* **2000**, *141*, F1–F6. [CrossRef]
52. Bulut, F.; Aktuğ, B.; Yaltırak, C.; Doğru, A.; Özener, H. Magnitudes of future large earthquakes near Istanbul quantified from 1500 years of historical earthquakes, present-day microseismicity and GPS slip rates. *Tectonophysics* **2019**, *764*, 77–87. [CrossRef]
53. Yaltırak, C. Marmara Denizi ve Çevresinde Tarihsel Depremlerin Yerleri ve Anlamı. *İTÜ Vakfı Dergisi* **2015**, *67*, 51–58.
54. Earthquake Hazards Program, U. Earthquake Magnitude, Energy Release, and Shaking Intensity. Available online: https://www.usgs.gov/programs/earthquake-hazards/earthquake-magnitude-energy-release-and-shaking-intensity (accessed on 14 November 2023).